

Showcasing Photonic Crystal Enhanced Microscopy (PCEM): A new label-free biosensor imaging approach to detect surface attachment of single dielectric and metal nanoparticles, representing one of the optics-based biosensor technologies developed by the Nano Sensors Group at the University of Illinois at Urbana-Champaign, directed by Professor Brian T. Cunningham. More information can be found at: nano.ece.illinois.edu.

Title: Single nanoparticle detection using photonic crystal enhanced microscopy

Photonic Crystal Enhanced Microscopy is a new label-free imaging technique utilizing a photonic crystal surface to detect surface attachment of individual dielectric and metal nanoparticles. Matching nanoparticle plasmon resonant frequency to the photonic crystal resonance substantially increases sensitivity of the approach.

As featured in:



See Brian T. Cunningham *et al.*,
Analyst, 2014, **139**, 1007.



www.rsc.org/analyst

Registered charity number: 207890

Single nanoparticle detection using photonic crystal enhanced microscopy†

 Cite this: *Analyst*, 2014, **139**, 1007

 Yue Zhuo,^a Huan Hu,^b Weili Chen,^b Meng Lu,^b Limei Tian,^c Hojeong Yu,^b Kenneth D. Long,^a Edmond Chow,^d William P. King,^{b,ef} Srikanth Singamaneni^c and Brian T. Cunningham^{*abd}

We demonstrate a label-free biosensor imaging approach that utilizes a photonic crystal (PC) surface to detect surface attachment of individual dielectric and metal nanoparticles through measurement of localized shifts in the resonant wavelength and resonant reflection magnitude from the PC. Using a microscopy-based approach to scan the PC resonant reflection properties with 0.6 μm spatial resolution, we show that metal nanoparticles attached to the biosensor surface with strong absorption at the resonant wavelength induce a highly localized reduction in reflection efficiency and are able to be detected by modulation of the resonant wavelength. Experimental demonstrations of single-nanoparticle imaging are supported by finite-difference time-domain computer simulations. The ability to image surface-adsorption of individual nanoparticles offers a route to single molecule biosensing, in which the particles can be functionalized with specific recognition molecules and utilized as tags.

 Received 19th October 2013
 Accepted 17th December 2013

DOI: 10.1039/c3an02295a

www.rsc.org/analyst

Introduction

Nanoparticles (NP) prepared from dielectric,¹ semiconductor,² metal,³ and magnetic⁴ materials have recently become important elements of biosensor technology due to the ability to prepare their surfaces with ligands that enable them to recognize specific target molecules, and their ability to interact with electromagnetic fields in useful ways.^{5–15} For example, nanoparticles with dielectric permittivity greater than that of water may be used as secondary tags for enhancing the signals from resonant optical biosensors,¹⁶ while magnetic nanoparticles are used to facilitate particle manipulation while at the same time providing a mass amplification tag for acoustic biosensors.¹⁷ Likewise, metallic nanoparticles, comprised of silver or gold, couple with external illumination sources to generate surface plasmons, which are used to enhance local electric fields on the nanoparticle surface.^{18,19} While many biosensing approaches

are capable of sensing the adsorption of large numbers of nanoparticles,²⁰ several approaches are capable of detecting the presence of a single nanoparticle, if the particle is adsorbed to a specific active location.^{21–25} Due to the difficulty of directing analytes to precise locations on a substrate surface where a biosensor has sensitivity, one approach to overcoming this limitation is to utilize a biosensor surface in which the entire surface area is active as a sensor. Through the use of an imaging detection approach, the adsorption of analyte upon any region within the field of view may be measured. Imaging-based biodetection utilizing optical sensors has been demonstrated using surface plasmon resonance,^{26–28} photonic crystal biosensors,^{29–33} and dielectric thin film interference sensors.^{34–37} Such approaches are advantageous because analytes that produce highly localized changes in dielectric permittivity, such as cells, virus particles, or nanoparticles, may be detected, with the potential to observe the attachment of individual targets.

In this work, we apply a recently developed form of microscopy, termed “Photonic Crystal Enhanced Microscopy” (PCEM) to imaging the attachment of dielectric and metallic nanoparticles upon a photonic crystal (PC) surface. While our initial demonstration of PCEM described imaging the spatial distribution and time evolution of live cell attachment strength to a functionalized PC surface with 0.6 μm pixel resolution,³⁸ here we report the detection of nanoparticles that are smaller than the pixel size. We demonstrate that metallic Au nanoparticles or nanorods produce highly localized effects upon the PC resonant reflection spectrum that enable individually attached particles to be easily observed by two distinct mechanisms, for particles as small as $\sim 65 \text{ nm} \times 30 \text{ nm}$. We observe that the dielectric

^aDepartment of Bioengineering, University of Illinois at Urbana-Champaign, Urbana, Illinois 61801, USA. E-mail: bcunning@illinois.edu

^bDepartment of Electrical and Computer Engineering, University of Illinois at Urbana-Champaign, Urbana, Illinois 61801, USA

^cDepartment of Mechanical Engineering and Materials Science, Washington University in St. Louis, St. Louis, Missouri 63130, USA

^dMicro and Nanotechnology Laboratory, University of Illinois at Urbana-Champaign, Urbana, Illinois 61801, USA

^eDepartment of Mechanical Science and Engineering, University of Illinois at Urbana-Champaign, Urbana, Illinois 61801, USA

^fDepartment of Materials Science and Engineering, University of Illinois at Urbana-Champaign, Urbana, Illinois 61801, USA

† Electronic supplementary information (ESI) available. See DOI: 10.1039/c3an02295a

permittivity of particles results in a local shift in the resonant wavelength of the PC, while the optical absorption of nanoparticles results in a localized reduction in the resonant reflectivity magnitude. We anticipate the use of dielectric or metallic nanoparticles as functionalized tags in “sandwich” style assays, that can be used to visualize the presence of individual captured analyte biomolecules upon a PC surface. PCEM nanoparticle imaging offers an attractive alternative to detection of fluorescent nanoparticles, as PCEM requires only low power broadband illumination, does not suffer from photobleaching, can provide long-term time-course data, and can be utilized for any type of nanoparticle tag.

PC biosensor design and operating principle

PC biosensors have recently been demonstrated as a highly versatile technology for a variety of label-free assays including high-throughput screening of small molecule–protein

interactions, characterization of protein–protein interactions, and measurement of cell attachment modulation by drugs.^{30,31,39} A PC is a sub-wavelength grating structure consisting of a periodic arrangement of a low refractive index material coated with a high refractive index layer (Fig. 1a). When the PC is illuminated with a broadband light source, high order diffraction modes couple light into and out of the high index layer, destructively interfering with the zeroth-order transmitted light.²⁷ At a particular resonant wavelength and incident angle, complete interference occurs and no light is transmitted, resulting in nearly 100% reflection efficiency. The resonant wavelength is modulated by the addition of biomaterial upon the PC surface, resulting in a shift to a higher wavelength. The electromagnetic standing wave that is generated at the PC surface during resonant light coupling inhibits lateral propagation, thus enabling neighboring regions on the PC surface to display a distinct resonant wavelength that is determined only by the density of biomaterial attached at that precise location. By measuring the resonant peak wavelength value (PWV) on a pixel-by-pixel basis over a PC surface, an image

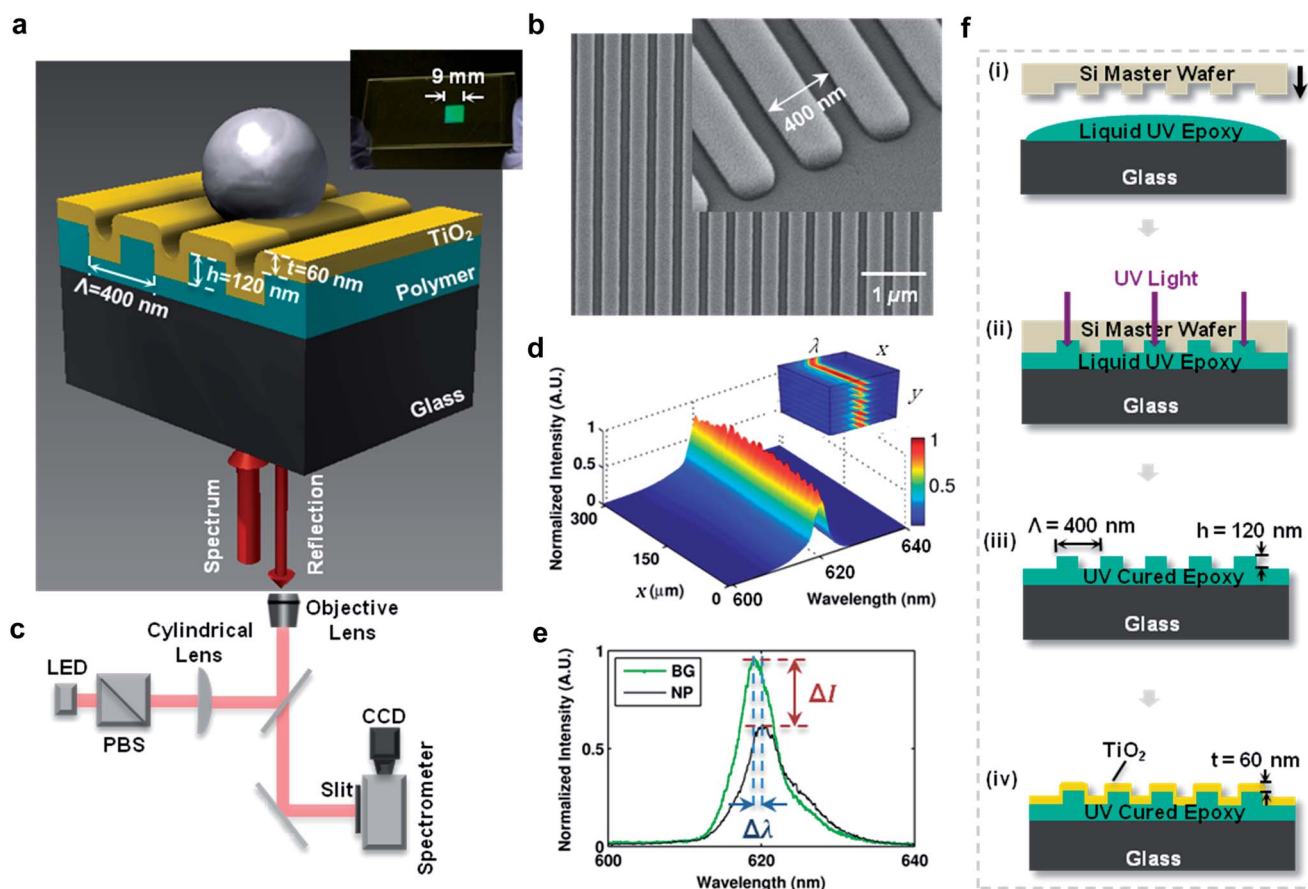


Fig. 1 Principle of Photonic Crystal Enhanced Microscopy (PCEM). (a) Schematic diagram of a nanoparticle attached to a photonic crystal (PC) surface. Inset: photo of a PC fabricated on a glass cover slip. (b) Scanning electron micrograph of the PC surface. Inset: Zoomed in image. (c) Instrument schematic of the PCEM. (d) Normalized spectrum image (surface plot). Inset: PCEM-acquired 3D spectrum data. (e) Example spectrum with a peak wavelength value (PWV) shift and a peak intensity value (PIV) change with/without one detected nanoparticle (BG-background, NP-nanoparticle) on the PC surface. (f) Schematic diagram of the PC fabrication procedure: (i) the process begins with depositing a thin layer of liquid UV epoxy polymer between a Si wafer template and a glass substrate. (ii) The epoxy is converted to a solid with UV light exposure. (iii) The template is peeled away and the grating pattern is transferred to the glass (iv) A thin layer of sputter-deposited TiO₂ film is applied over the grating structure.

of nanoparticle attachment may be recorded. PWV images of the PC may be gathered by illuminating the structure with low intensity collimated broadband light through the transparent substrate, while the front surface of the PC is immersed in aqueous media.

The PC sensors used in this study were fabricated using a low-cost nanoreplica molding approach (Fig. 1f) that has been described previously.²⁹ Briefly, a silicon wafer molding template with a negative volume image of the desired PC grating structure (period = 400 nm, depth = 120 nm) was fabricated using deep-UV lithography and reactive ion etching. Liquid UV-curable epoxy was pressed between a glass cover slip (0.17 mm thick) and the silicon wafer, and was subsequently cured to a solid using a high intensity UV lamp. The hardened epoxy preferentially adhered to the glass substrate and was peeled away from the silicon wafer, leaving a replica of the silicon mold. A thin TiO₂ layer ($t \sim 60$ nm) was deposited *via* reactive RF sputtering (PVD 75, Kurt Lesker) providing the high-refractive index coating. Fig. 1b presents a scanning electron micrograph of the replica-molded sensor after dielectric coating that shows excellent uniformity across the PC surface. The grating height is ~ 80 nm and the roughness on PC surface is $4.3 \text{ nm} \pm 1.0 \text{ nm}$ (top) and $6.6 \text{ nm} \pm 1.4 \text{ nm}$ (gap between the teeth) for an area of $100 \text{ nm} \times 100 \text{ nm}$, as measured by atomic force microscopy (AFM). The PC is designed to resonantly reflect a wavelength of $\lambda \sim 620$ nm, when covered by aqueous media.

PCEM instrument

A schematic diagram of the PCEM instrument is shown in Fig. 1c. The system is built upon the body of a standard microscope (Carl Zeiss Axio Observer Z1), but in addition to ordinary bright field imaging, a second illumination path is provided from a fiber-coupled broadband light-emitting diode (LED) (Thorlabs M617F1, $600 < \lambda < 650$ nm). The fiber output is collimated and filtered by a polarizing beamsplitter (PBS) cube to illuminate the PC with light that is polarized with its electric field vector oriented perpendicular to the grating lines. The polarized beam is focused by a cylindrical lens ($f = 200$ mm) to form a linear beam at the back focal plane of the objective lens ($10\times$ or $40\times$ Zeiss). After passing through the objective lens, the orientation of the line-shaped beam is rotated to illuminate the PC from below at normal incidence. The reflected light is projected, *via* a side port of the inverted microscope and a zoom lens ($1.6\times$), onto a narrow slit aperture at the input of an imaging spectrometer. The width of the adjustable slit was set to $30 \mu\text{m}$ for the work reported here. Using this method, reflected light is collected from a linear region of the PC surface, where the width of the imaged line, $1.2 \mu\text{m}$, is determined by the width of the entrance slit of the imaging spectrometer and the magnification power of the objective lens. The system incorporates a grating-based spectrometer (Acton Research) with a 512×512 pixel CCD camera (Photometrics Cascade 512).

The line of reflected light, containing the resonant biosensor signal, is diffracted by the grating within the spectrometer (300 lines per mm) to produce a spatially resolved spectrum for each point along the line. Therefore, each pixel across the line is

converted to a resonant reflection spectrum (Fig. 1e), containing a narrow bandwidth ($\Delta\lambda \sim 4$ nm) reflectance peak from the PC. The PWV of each peak is determined by fitting the spectrum to a 2nd order polynomial function, and then mathematically determining the maximum wavelength of the function. By fitting all 512 spectra, in a process that takes 20 ms, a line comprised of 512 pixels is generated that represents one line of a PWV image of the PC surface (Fig. 1d). With a $10\times$ objective lens and an effective magnification of $26\times$, each pixel in the line represents a $\sim 0.6 \mu\text{m}$ width on the PC surface and 512 such pixels cover a total width of $\sim 300 \mu\text{m}$ (x dimension). To generate a two-dimensional PWV image of the PC surface, a motorized stage (Applied Scientific Instruments, MS2000) translates the sensor along the axis perpendicular to the imaged line (y dimension) in increments of $0.6 \mu\text{m}$ per step. Using this technique, a series of lines are assembled into an image (Fig. 1d inset) at a rate of 0.1 s per line and the same area on the PC surface can be scanned repeatedly. Each image is comprised of 512 by n pixels, where n can be selected during each scan session, and each pixel represents a $0.6 \times 0.6 \mu\text{m}^2$ region of the PC surface. A biosensor experiment involves measuring shifts in PWV and/or shifts in the resonant Peak Intensity Value (PIV).

Results

Computer simulations of nanoparticle interaction with resonant electric fields on the PC

We applied numerical finite-difference time-domain (FDTD) computer simulations of the PC structure with a deposited single dielectric or metallic nanoparticle,⁴⁰ to predict the effect of the particle on the local reflectance spectrum and to visualize the redistribution of electromagnetic fields (Fig. 2). Two periods of the device are simulated, with periodic boundary conditions applied to the x extents. Using the physical dimensions of the fabricated device to specify the modeled structure, FDTD predicts a resonant reflection wavelength of $\lambda = 620$ nm and a reflection efficiency $I = 96\%$. The simulated electric-field power distributions ($|E|^2$) of the PC at the resonant wavelength with/without a TiO₂ (500 nm) and Au (100 nm) nanoparticle are shown in Fig. 2a and b, in which a uniform plane wave illuminates the structure at normal incidence with a magnitude of $E = 1 \text{ V m}^{-1}$. The “Empty” PC simulation (Fig. 2a) demonstrates the expected establishment of an evanescent electric field at the surface with enhanced electric field magnitude that develops due to the formation of electric field standing waves. Fig. 2b demonstrates the presence of TiO₂ or Au nanoparticles at two slightly different locations on the PC biosensor surface (deposited on top of a grating tooth, or at the bottom of the gap between teeth), respectively. The presence of nanoparticles (at the bottom of gap between teeth) induces substantial changes in near-field distributions and results in a shift of resonance wavelength by $\Delta\lambda = 1.04$ nm (TiO₂) and $\Delta\lambda = 0.14$ nm (Au). The predicted reduction in the resonant intensity by the presence of the TiO₂ and Au nanoparticles is $\Delta I = 60\%$ and $\Delta I = 13\%$, respectively (Fig. 2c).

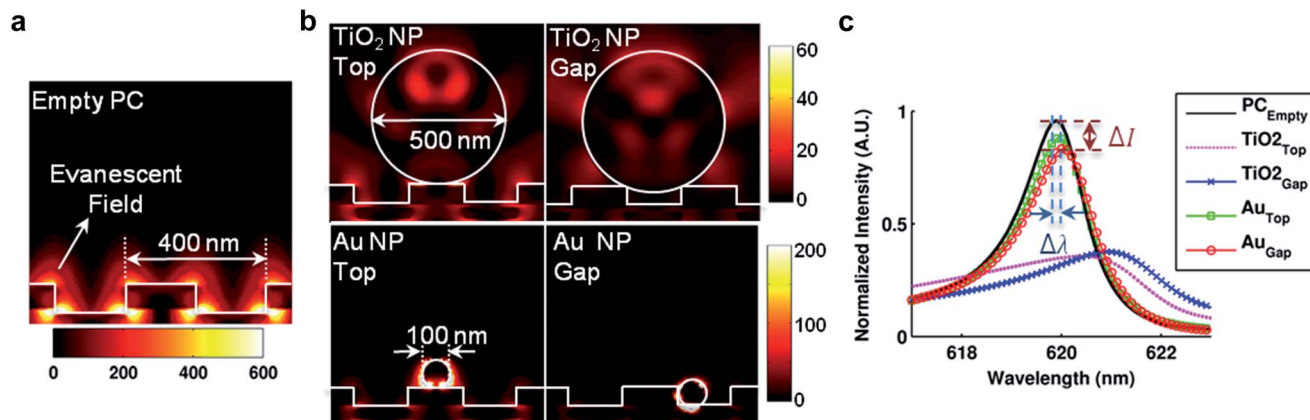


Fig. 2 Computer simulations of reflection and near field distributions of the PC with and without nanoparticles (NP). The simulations demonstrate the finite-difference time-domain (FDTD) computed electric-field power distributions (in units of $V^2 m^{-2}$) for different conditions: (a) empty PC; (b) 500 nm TiO_2 NP and 100 nm Au NP at two slightly different locations on a PC surface (deposited on top of a grating tooth, denoted by "Top", or at the bottom of the gap between teeth, denoted by "Gap"). (c) FDTD-computed reflection spectra of NP on the PC surface, predicting a clearly measurable change in reflectance wavelength and intensity with/without nanoparticles.

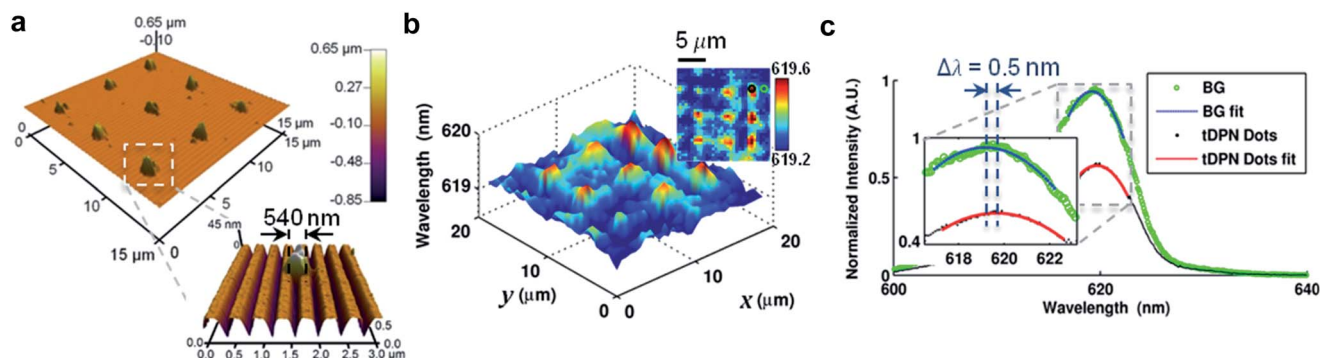


Fig. 3 PCEM detection of nano-dots printed by thermal Dip-Pen Nanolithography (tDPN). (a) Atomic force microscopy (AFM) images of tDPN-printed 3×3 arrays of nano-dots. Inset: Zoomed in AFM images of one $540 \times 540 \times 40$ nm³ tDPN nano-dot. (b) PCEM reflected PWV image of the tDPN nano-dots displayed in a 3D surface plot within a 20×20 μm^2 field of view. Inset: 2D PWV image, demonstrating the ability of PCEM to resolve PWV differences caused by single nano-dot attachment to the PC surface. (c) Normalized spectrum of a representative tDPN nano-dot (black line) and a background pixel (green line). Inset: Zoomed in image of the spectrum with 2D polynomial fitting (tDPN nano-dot fitting in red line, background fitting in blue line), indicating a PWV shift of $\Delta\lambda = 0.5$ nm.

Single dielectric nanoparticle detection

To facilitate investigation of PCEM's ability to detect individual nanoparticles with tightly controlled spatial distribution and size, we first sought to intentionally deposit patterns of polymer spots using thermal Dip-Pen Nanolithography (tDPN).^{41–44} The principle of tDPN is to use a heated AFM tip to deposit polystyrene (PS) nano-patterns on the PC surface. We printed 3×3 arrays of PS dots (540 nm diameter, 40 nm height, and 5 μm gaps between dots) on a PC surface confirmed by AFM imaging (Fig. 3a). Fig. 3c displays the measured PWV images of the tDPN printed nano-dots. From the spectrum of two neighboring pixels (marked with black and green circles in Fig. 3b inset image), we can visualize a peak-wavelength shift of $\Delta\lambda = 0.5$ nm caused by the nano-dots (black line), compared to the background pixel (green line) (Fig. 3c). The PCEM-measured diameter (ESI, Fig. 1b†) closely matches the AFM-measured diameter (ESI, Fig. 1a†), except that the nano-dot dielectric permittivity

slightly increases the PWV of surrounding pixels. It is important to note that the nano-dots are approximately the same size as the pixel, so a single nano-dot can partially occupy several adjacent pixels at the same time.

Having demonstrated the ability to observe and resolve dielectric-based polymer nanoparticles that were intentionally patterned on the PC, we next sought to detect dielectric TiO_2 nanoparticles of approximately the same size, but distributed randomly on the PC surface (Fig. 4a–c). The PC surface was prepared by cleaning with isopropanol and deionized (DI) water, followed by drying using N_2 . To further facilitate nanoparticle attachment, the PC was oxygen-plasma treated for five minutes after cleaning. The TiO_2 nanoparticle is 500 nm in diameter (Microspheres-nanospheres, #220374-10) and incubated in DI water on the PC surface for two hours and then imaged *via* PCEM. Fig. 4c shows the measured PCEM spectra for two neighboring pixels (black line represents the location of an

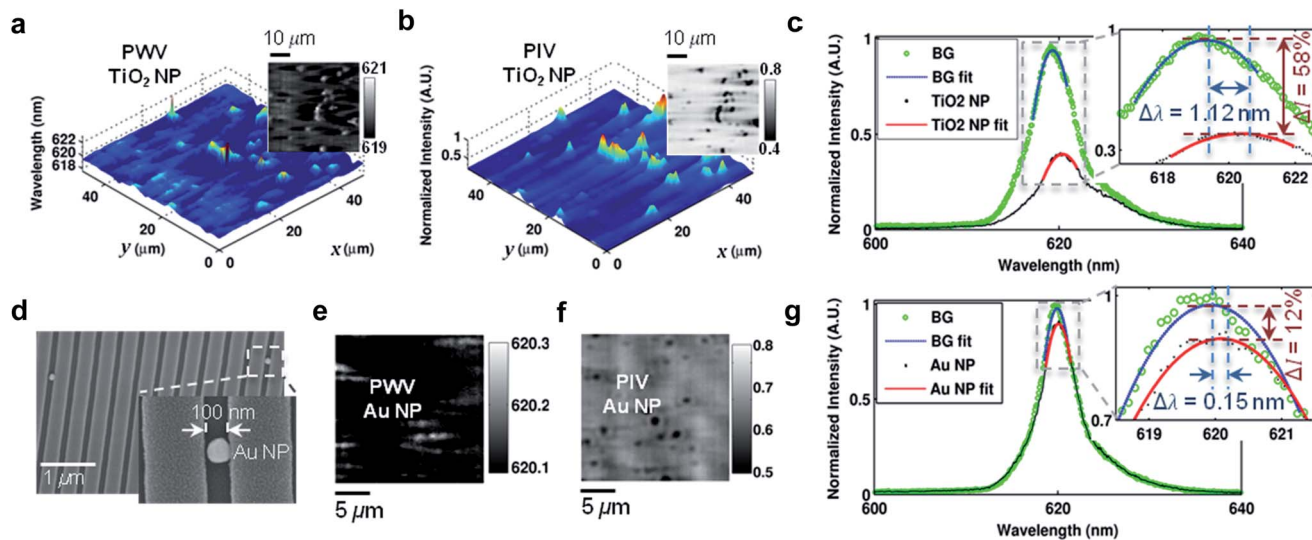


Fig. 4 PCEM detection of randomly distributed TiO_2 and Au nanoparticles (NP). (a) PCEM-detected PWV image of the TiO_2 NP displayed in a 3D surface plot. Inset: 2D PWV image in gray scale. (b) PCEM detected PIV image of the TiO_2 NP displayed in a 3D surface plot (inverted for comparison). Inset: 2D PIV image in gray scale. (c) Normalized spectrum of a 500 nm TiO_2 NP and a background pixel. Inset: Zoomed in image of the normalized spectrum with 2D polynomial fitting (TiO_2 NP fitting in red line, background fitting in blue line), indicating a PWV shift of $\Delta\lambda = 1.12$ nm and a PIV reduction of $\Delta I = 58\%$ when the NP is present. (d) Scanning electron micrograph of the Au NP on PC surface. Inset: Zoomed in image. PCEM detected (e) PWV image and (f) PIV image of the Au NP displayed in 2D with gray scale. (g) Normalized spectrum of a 100 nm Au NP and a background pixel. Inset: zoomed in image of the normalized spectrum with 2D polynomial fitting (Au NP fitting in red line, background fitting in blue line), indicating a PWV shift of $\Delta\lambda = 0.15$ nm and a PIV reduction of $\Delta I = 12\%$ when the NP is present.

adsorbed TiO_2 nanoparticle, while the green line represents a background pixel without an adsorbed nanoparticle). The TiO_2 nanoparticle induces a highly localized and easily observed peak-wavelength shift of $\Delta\lambda = 1.12$ nm and a peak-intensity reduction of $\Delta I = 58\%$. Calculating these values for each pixel in the field of view allows us to form the PWV (Fig. 4a) and PIV (Fig. 4b) images for several independently adsorbed TiO_2 nanoparticles.

Single metal nanoparticle detection

We next sought to detect the presence of surface-adsorbed gold (Au) nanoparticles of approximately 100 nm diameter (Sigma, #742031-25ML), distributed randomly on the PC surface (Fig. 4d–g). The PC surface was prepared as described above. Scanning electron microscopy (SEM) images of single gold nanoparticles on the PC surface are shown in Fig. 4d, demonstrating that the particles are present as distinct individuals, rather than as clusters. Individual Au nanoparticles were observed to cause a pronounced change in the resonant reflection spectrum for only the pixels of the PCEM image where the particle was adsorbed. We observe a shift in the peak reflectance wavelength of $\Delta\lambda = 0.15$ nm, and a reduction in the peak reflectance intensity of $\Delta I = 12\%$. The PWV shift (Fig. 4e) is a result of the increased real part of the dielectric permittivity of gold with respect to the surrounding water medium, while the decrease in PIV (Fig. 4f) is caused by the imaginary part of the refractive index of gold at the resonant wavelength of the PC, which results in highly localized optical absorption. The localized nature of the effect can be observed by comparing spectra from neighboring pixels (black line represents a pixel from the

location of an adsorbed Au nanoparticle, while the green line represents the background region without an Au particle), as shown in Fig. 4g. The dynamic detection of 100 nm Au (Video 1†) and TiO_2 (Video 2†) nanoparticles shows the random adsorption, desorption, and re-adsorption of single nanoparticles in DI water on a PC surface.

Detection of protein–protein binding with single metal nanorods

Additionally, we studied the biosensor's ability to detect target bioanalytes binding with immobilized antibody on the PC biosensor surface (with a $40\times$ objective lens). To match the PC resonant wavelength, we synthesized gold nanorods (AuNR) with resonant optical absorption spectra around ~ 620 nm (ESI, Fig. 3b† demonstrates the transmission electron microscopy (TEM) image of AuNR). The size of the synthesized AuNR is $66.7 \text{ nm} \pm 5.5 \text{ nm}$ in length and $30.7 \text{ nm} \pm 4.0 \text{ nm}$ in diameter (as analyzed in TEM images from 56 AuNR). Then we employed Rabbit IgG (IgG henceforth) as model capture biomolecule and anti-Rabbit IgG (anti-IgG) as model target bioanalyte to demonstrate the detection of antibody–antigen binding (Fig. 5a). ESI, Fig. 3a† illustrates the binding of biomolecules to target bioanalytes attached to the PC biosensor surface. In this setup, thiol-terminated polyethylene glycol (SH-PEG), a hydrophilic polymer, serves as a flexible linker to increase the accessibility of IgG to target bioanalyte.^{45,46} The AuNR–IgG conjugates were prepared by functionalizing AuNR with SH-PEG–IgG molecules (ESI, Fig. 3c†). Subsequently, anti-IgG was adsorbed onto the PC biosensor surface by exposing the PC to anti-IgG solution followed by thorough rinsing with phosphate

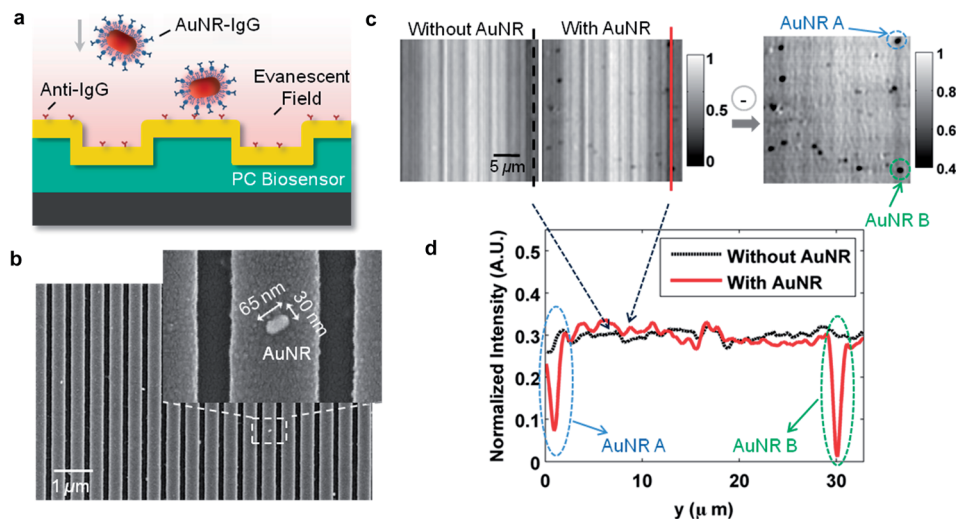


Fig. 5 PCEM detection of protein–protein binding. (a) Schematic illustration of the attachment of AuNR–IgG (AuNR conjugated with SH–PEG–IgG) on the PC biosensor surface. (b) SEM images of AuNR–IgG attached to the PC biosensor surface. Inset: Zoomed in image. (c) PCEM detected PIV images (in gray scale) and the difference between without and with AuNR–IgG on the PC surface. (d) Two representative cross-section lines of the normalized intensity images with/without two AuNRs–IgG on the PC surface.

buffered saline to remove the weakly adsorbed antibody. Exposing the PC surface to AuNR–IgG conjugates resulted in specific binding to anti-IgG (SEM images shown in Fig. 5b), which can be detected as a PIV reduction in the area absorbed with AuNR. Fig. 5c shows the mathematical difference between two PIV images taken before and after AuNR–IgG attachment and selected cross-section lines in the PIV images (Fig. 5d). It demonstrates that PCEM can successfully detect the intensity reduction in presence of AuNR–IgG.

Discussion

The PCEM detection instrument configuration with $10\times$ objective lens described in this work provides a field of view of $300 \times 300 \mu\text{m}^2$, comprised of an array of $0.6 \times 0.6 \mu\text{m}^2$ pixels, determined by the combined effects of the objective numerical aperture, the scan increment and the pixel size of the CCD camera within the imaging spectrometer. The resolution with which individual nanoparticles may be identified as distinct objects is partially determined by the above instrument parameters, but is also influenced by the ability of the PC surface to confine the lateral propagation of its resonant electromagnetic field standing wave. Ultimately, the resolution of our approach will not be capable of exceeding the diffraction limit, which for a wavelength of $\lambda = 620 \text{ nm}$ and our numerical aperture of 0.25, is $d = 1518 \text{ nm}$. The resolution of the optical system can be calculated using Abbe's formula

$$d = \frac{0.612 \lambda}{n \sin \alpha}, \quad (1)$$

where λ is the wavelength of the imaging radiation; n is the medium refraction index between the light source and the lens; α denotes half of the angular aperture of the light source. The $n \sin \alpha$ term in Abbe's formula represents the numerical aperture (N.A.).

Using the PCEM images of individual nanoparticles that are smaller than the pixel size, we are able to characterize the extent to which a nanoparticle can influence the resonant properties of neighboring pixels, by observing how the resonant reflectance properties are influenced as one moves laterally across the PC surface. Because the location of a nanoparticle within a pixel is random, it is important to note that a particle will always be within a diffraction limited distance of up to five adjacent pixels, and thus we would not expect to observe a single pixel with a shift in wavelength or reflected intensity. The distribution of PWV and PIV shift in the horizontal and vertical directions surrounding individual TiO_2 nanoparticles in our images are plotted in ESI, Fig. 2a and b.† The data reveals that a 500 nm diameter surface-adsorbed TiO_2 nanoparticle results in a positive shift in PWV that extends approximately $6 \mu\text{m}$ in the horizontal direction (perpendicular to the PC grating lines) and $5 \mu\text{m}$ in the vertical direction (parallel to the PC grating lines). Calculating the full-width at half-maximum (FWHM) of the point spread function of ten separate TiO_2 nanoparticles results in a mean $\text{FWHM} = 1.56 \mu\text{m}$, and a standard deviation of $0.26 \mu\text{m}$ in the horizontal direction and $\text{FWHM} = 1.20 \pm 0.28 \mu\text{m}$ in the vertical direction. Thus, for two neighboring nanoparticles to be observed independently, they must be separated by at least $2 \cdot \text{FWHM}$, approximately $3.2 \mu\text{m}$. Interestingly, PIV-based PCEM images of the same TiO_2 nanoparticles measured using the reduction in reflection efficiency results in slightly improved resolution. We measured FWHM of $0.95 \pm 0.09 \mu\text{m}$ for PIV images in the horizontal direction, and FWHM of $0.96 \pm 0.39 \mu\text{m}$ in the vertical direction. Results are summarized in ESI, Table 1.†

Similar results are obtained when observing the point spread function of surface-adsorbed 100 nm Au nanoparticles. Observation of the variation in PWV and PIV in the horizontal and vertical directions surrounding an individual Au nanoparticle, plotted in ESI, Fig. 2c and d,† results in a FWHM of $1.15 \pm 0.05 \mu\text{m}$ for

PIV images in the horizontal direction, and FWHM of $0.97 \pm 0.07 \mu\text{m}$ in the vertical direction. We observe that surface-adsorbed dielectric and metallic nanoparticles extend their influence to surrounding regions of the PC surface for approximately the same distance.

Our observations of the resolution of PCEM images of isolated nanoparticles (100 nm Au NP) suggest that the resonant electric field standing waves of any particular region of the PC are influenced by surrounding regions that are $\sim 3 \mu\text{m}$ away. Fundamentally, this distance is determined by the design of the PC, as discussed in previous work.⁴⁷ The periodic grating structure results in partial back-reflection of resonantly coupled light that has its propagation vector oriented parallel to the PC surface. The modulation of the grating, determined by the grating step height, the thickness of the TiO_2 , and the refractive index contrast of the TiO_2 /polymer/water interfaces, determines the efficiency with which laterally-directed light is folded back onto itself. Because the FWHM is $\sim 1200 \text{ nm}$, and the grating period is 400 nm , we estimate that ~ 6 back reflections are required to confine resonantly coupled light for the PC design used in this work. This factor, rather than the diffraction limit, provides the current resolution limitation of our approach. We have previously shown that PC structures with lower quality (Q) factor (broader resonant bandwidth) provide greater lateral confinement, so this may be a direction for future investigation.

A point of interest for detection of metallic nanoparticles is the overlap between the PC resonant wavelength and the resonant optical absorption spectra of the nanoparticle. In this work, no effort was directed towards aligning these two values, except the last experiment using AuNR. Previous reports⁴⁸ demonstrate that Au nanoparticles of $\sim 100 \text{ nm}$ diameter have a broad absorption spectrum with a maximum of 572 nm , that extends to 700 nm . Thus, the PIV images are a result of quenching of the PC resonance due to absorption of light by the Au, but the absorption process used to obtain our PIV images is extremely inefficient. Despite this inefficiency, a single 100 nm Au nanoparticle provides easily measured resonant intensity contrast of $\sim 10\%$. While the contrast is expected to be further improved either by choosing nanoparticles with resonant absorption spectra that overlaps the resonant spectrum of the PC, or by designing a PC to more closely match the absorption of the nanoparticles. Our last experiment (Fig. 5) addresses this problem by applying the AuNR with approximately the same resonance wavelength with the PC surface.

Conclusions

In conclusion, we report the first application of PCEM to the detection of individual surface-adsorbed nanoparticles. We demonstrate that dielectric nanoparticles generate highly localized shift in the PC's reflected resonant wavelength, and that the wavelength shift is determined by the refractive index of the particle. Further, we show that metal nanoparticles not only shift the resonant wavelength, but through their optical absorption also substantially reduce the resonant reflection efficiency through quenching of the PC resonance. In this work, we characterized the image contrast and spatial resolution of

nanoparticle detection, demonstrating that nanoparticles must be separated from their neighbors by at least $4 \mu\text{m}$ to be uniquely observed. The results reported here lay the foundation for the use of nanoparticles as tags for biomolecular assays performed upon a PC surface and measured by a PCEM instrument. We envision the development of sandwich-style assays in which the PC surface is prepared with capture molecules for low-concentration analytes such as disease biomarkers or viral particles, where dielectric or metallic nanoparticle tags prepared with secondary antibodies can decorate the captured analyte. Such an approach will enable multiplexed detection of analytes with single-molecule resolution.

Materials and methods

PC biosensor simulation

A commercially available simulation package (FDTD, Lumerical Solutions, Inc.) is employed to simulate the distribution of excited electric field on the PC surface. The simulation results suggest the optimal physical parameters for PC grating structure. In this study, we choose a 1D UV-curable polymer structure ($n_{\text{poly}} = 1.5$) with a sufficiently high grating depth ($d = 120 \text{ nm}$) to confine the near field emission intensity. The grating period ($\Lambda = 400 \text{ nm}$) and duty cycle ($f = 50\%$) of the PC biosensor are selected to support high Q-factor resonant modes at the specific wavelength ($\lambda = 620 \text{ nm}$). The thickness ($t = 60 \text{ nm}$) of the deposited TiO_2 ($n_{\text{TiO}_2} = 2.4$) layer can be used to fine-tune the spectral location of the resonant modes. The corresponding evanescent field endures a penetration depth of approximate 200 nm into the adjacent media.

PC biosensor fabrication

The PC biosensor is fabricated by a nanoreplica molding approach (Fig. 1f). Deep-UV lithography and reactive ion etching are used to produce a silicon wafer molding template with a negative image of the desired grating profile. A thin layer of liquid epoxy polymer (UV-curable) is deposited between the wafer template and glass substrate and then cured to solid status by exposing it to a high intensity UV lamp. Therefore, the nano-patterned surface is transferred to the glass substrate through epoxy polymer after peeling off the wafer template. Finally, a thin TiO_2 film is sputtered over the grating structure using a reactive RF sputtering machine (PVD 75, Kurt Lesker).

PCEM imaging setup

A schematic diagram of PCEM imaging system is shown in Fig. 1c. To avoid light scattering and adsorption from the sample, PCEM imaging is performed *via* reflection from beneath the PC surface. The light source is a broadband LED (Thorlabs M617F1, $600 < \lambda < 650 \text{ nm}$) coupled with optical fiber. The microscope (Carl Zeiss Axio Observer Z1) is equipped with a $10\times$ or $40\times$ objective lens (Zeiss) plus an extra magnification lens ($1.6\times$). Following the extra lens, a narrow slit aperture ($\lambda = 620 \text{ nm}$, $\Delta\lambda = 30 \text{ nm}$) is incorporated with a grating-based spectrometer (Acton Research), which is connected to a CCD camera (Photometrics Cascade, 512×512 pixels). The

motorized stage (Applied Scientific Instruments, MS2000) enables scanning the sample with a selected increment (*e.g.* 0.6 μm) per step. In this study, the effective pixel size is 0.6 \times 0.6 μm^2 for a 10 \times objective lens.

PCEM data analysis

After acquiring the 3D data (*e.g.* 512³ cube) as shown in Fig. 1d, the signal/image processing is performed with computational software (Matlab, MathWorks). The signal is smoothed using a low-pass filter to remove acquisition noise. The spectrum signal for each pixel (Fig. 1e) is fitted to a 2nd order polynomial, which is used to extract the maximum wavelength and intensity.

Synthesis of gold nanorods

Gold nanorods (AuNR) were synthesized using a seed-mediated approach. Seed solution was prepared by adding 0.6 mL of an ice-cold sodium borohydride solution (10 mM) into 10 mL of 0.1 M cetyltrimethylammonium bromide (CTAB) and 2.5 \times 10⁻⁴ M chloroauric acid (HAuCl₄) solution under magnetic stirring at room temperature. The color of the seed solution changed from yellow to brown. Growth solution was prepared by mixing 95 mL of CTAB (0.1 M), 0.5 mL of silver nitrate (10 mM), 5 mL of HAuCl₄ (10 mM), and 0.55 mL of ascorbic acid (0.1 M) in the same order. The solution was homogenized by gentle stirring. To the resulting colorless solution, 0.12 mL of freshly prepared seed solution was added and aged for two weeks at room temperature. Prior to use, the AuNR solution was centrifuged at 10,000 rpm for 10 min to remove excess CTAB and redispersed in nanopure water (18.2 M Ω cm). The centrifugation procedure was repeated twice.

AuNR-IgG conjugates on PC biosensor surface

To a solution of heterobifunctional polyethylene glycol (SH-PEG-COOH) in water (37.5 μL , 20 μM , $M_w = 5000 \text{ g mol}^{-1}$, Jenkem Technology), 1-ethyl-3-(3-dimethylaminopropyl) carbodiimide (EDC, Thermo Scientific), and *N*-hydroxy succinimide (NHS, Thermo Scientific) with the same molar ratio as SH-PEG-COOH were added followed by shaking for 1 h. The pH of the above reaction mixture was adjusted to 7.4 by adding 10 \times concentrated phosphate buffered saline buffer solution, followed by the addition of rabbit immunoglobulin G (IgG) (10 μL , 75 μM , $M_w = 150 \text{ kDa}$, Thermo Scientific). The reaction mixture was incubated for 2 h, and then filtered to remove any byproduct during the reaction using a 50 kDa filter. The final SH-PEG-IgG conjugates solution (0.75 μM) was obtained after washing with phosphate buffered saline buffer (pH 7.4) twice. AuNR-IgG conjugates solution was prepared by adding 50 μL SH-PEG-IgG conjugates solution to 1 mL twice centrifuged AuNR solution with incubation for 1 h. The amount of SH-PEG-IgG was optimized to obtain maximum coverage of IgG on AuNR surface. Then the PC surface was exposed to AuNR-IgG conjugates solution for 30 min, followed by rinsing with DI water to remove the loosely bound nanorods.

Acknowledgements

This work is supported by National Science Foundation Grant CBET 11-32301. The authors would like to thank the Nano Sensor Groups (NSG) and staff in Micro and Nanotechnology Laboratory (MNLT), the Center for Agricultural, Biomedical, and Pharmaceutical Nanotechnology (CABPN) at University of Illinois at Urbana-Champaign for their support.

References

- 1 K. T. Thurn, T. Paunesku, A. Wu, E. M. Brown, B. Lai, S. Vogt, J. Maser, M. Aslam, V. Dravid, R. Bergan and G. E. Woloschak, *Small*, 2009, **5**, 1318–1325.
- 2 D. Ishii, K. Kinbara, Y. Ishida, N. Ishii, M. Okochi, M. Yohda and T. Aida, *Nature*, 2003, **423**, 628–632.
- 3 R. A. Sperling, P. R. Gil, F. Zhang, M. Zanella and W. J. Parak, *Chem. Soc. Rev.*, 2008, **37**, 1896–1908.
- 4 P. M. Winter, A. M. Morawski, S. D. Caruthers, R. W. Fuhrhop, H. Zhang, T. A. Williams, J. S. Allen, E. K. Lacy, J. D. Robertson, G. M. Lanza and S. A. Wickline, *Circulation*, 2003, **108**, 2270–2274.
- 5 J. N. Anker, W. P. Hall, O. Lyandres, N. C. Shah, J. Zhao and R. P. Van Duyne, *Nat. Mater.*, 2008, **7**, 442–453.
- 6 A. Mitra, B. Deutsch, F. Ignatovich, C. Dykes and L. Novotny, *ACS Nano*, 2010, **4**, 1305–1312.
- 7 R. V. Olkhov, J. D. Fowke and A. M. Shaw, *Anal. Biochem.*, 2009, **385**, 234–241.
- 8 C. Novo, A. M. Funston and P. Mulvaney, *Nat. Nanotechnol.*, 2008, **3**, 598–602.
- 9 G. J. Nusz, S. M. Marinakos, A. C. Curry, A. Dahlin, F. Hook, A. Wax and A. Chilkoti, *Anal. Chem.*, 2008, **80**, 984–989.
- 10 K. M. Mayer, F. Hao, S. Lee, P. Nordlander and J. H. Hafner, *Nanotechnology*, 2010, **21**, 255503.
- 11 K. M. Mayer, S. Lee, H. Liao, B. C. Rostro, A. Fuentes, P. T. Scully, C. L. Nehl and J. H. Hafner, *ACS Nano*, 2008, **2**, 687–692.
- 12 T. Sannomiya, C. Hafner and J. Voros, *Nano Lett.*, 2008, **8**, 3450–3455.
- 13 S. M. Marinakos, S. Chen and A. Chilkoti, *Anal. Chem.*, 2007, **79**, 5278–5283.
- 14 C. Sonnichsen, B. M. Reinhard, J. Liphardt and A. P. Alivisatos, *Nat. Biotechnol.*, 2005, **23**, 741–745.
- 15 S. Schultz, D. R. Smith, J. J. Mock and D. A. Schultz, *Proc. Natl. Acad. Sci. U. S. A.*, 2000, **97**, 996–1001.
- 16 R. C. Bailey, J. M. Nam, C. A. Mirkin and J. T. Hupp, *J. Am. Chem. Soc.*, 2003, **125**, 13541–13547.
- 17 M. F. Miller, B. P. Masters and M. E. Lundstrom, *US Pat.*, 2007, US 7300631 B2.
- 18 Y. Wang, H. Chen, S. Dong and E. Wang, *J. Chem. Phys.*, 2006, **125**, 44710.
- 19 L. Cognet, C. Tardin, D. Boyer, D. Choquet, P. Tamarat and B. Lounis, *Proc. Natl. Acad. Sci. U. S. A.*, 2003, **100**, 11350–11355.
- 20 J. Lee, W. Shen, K. Payer, T. P. Burg and S. R. Manalis, *Nano Lett.*, 2010, **10**, 2537–2542.

- 21 M. R. Lee and P. M. Fauchet, *Opt. Lett.*, 2007, **32**, 3284–3286.
- 22 J. Zhu, S. K. Ozdemir, Y. Xiao, L. Li, L. He, D. Chen and L. Yang, *Nat. Photonics*, 2010, **4**, 46–49.
- 23 A. Gupta, D. Akin and R. Bashir, *Appl. Phys. Lett.*, 2004, **84**, 1976–1978.
- 24 M. L. Juan, R. Gordon, Y. Pang, F. Eftekhari and R. Quidant, *Nat. Phys.*, 2009, **5**, 915–919.
- 25 A. Kotnala, D. DePaoli and R. Gordon, *Lab Chip*, 2013, **13**, 4142–4146.
- 26 S. Nie and S. R. Emory, *Science*, 1997, **275**, 1102–1106.
- 27 W. Zhang, L. Huang, C. Santschi and O. J. F. Martin, *Nano Lett.*, 2010, **10**, 1006–1011.
- 28 S. Wang, X. Shan, U. Patel, X. Huang, J. Lu, J. Li and N. Tao, *Proc. Natl. Acad. Sci. U. S. A.*, 2010, **107**, 16028–16032.
- 29 B. T. Cunningham, B. Lin, J. Qiu, P. Li, J. Pepper and B. Hugh, *Sens. Actuators, B*, 2002, **85**, 219–226.
- 30 B. T. Cunningham, P. Li, B. Lin and J. Pepper, *Sens. Actuators, B*, 2002, **81**, 316–328.
- 31 B. T. Cunningham, P. Li, S. Schulz, B. Lin, C. Baird, J. Gerstenmaier, C. Genick, F. Wang, E. Fine and L. Laing, *J. Biomol. Screening*, 2004, **9**, 481–490.
- 32 N. Ganesh, I. D. Block and B. T. Cunningham, *Appl. Phys. Lett.*, 2006, **89**, 023901–023903.
- 33 J. O. Grepstad, P. Kaspar, O. Solgaard, I. R. Johansen and A. S. Sudbo, *Opt. Express*, 2012, **20**, 7954–7965.
- 34 R. Vedula, G. Daaboul, A. Reddington, E. Ozkumur, D. A. Bergstein and M. S. Unlu, *J. Mod. Opt.*, 2010, **57**, 1564–1569.
- 35 G. G. Daaboul, A. Yurt, X. Zhang, G. M. Hwang, B. B. Goldberg and M. S. Unlu, *Nano Lett.*, 2010, **10**, 4727–4731.
- 36 M. R. Monroe, G. G. Daaboul, A. Tuysuzoglu, C. A. Lopez, F. F. Little and M. S. Unlu, *Anal. Chem.*, 2013, **85**, 3698–3706.
- 37 S. Person, B. Deutsch, A. Mitra and L. Novotny, *Nano Lett.*, 2011, **11**, 257–261.
- 38 W. Chen, K. D. Long, M. Lu, V. Chaudhery, H. Yu, J. S. Choi, J. Polans, Y. Zhuo, B. A. Harley and B. T. Cunningham, *Analyst*, 2013, **138**, 5886–5894.
- 39 P. C. Mathias, S. I. Jones, H. Y. Wu, F. Yang, N. Ganesh, D. O. Gonzalez, G. Bollero, L. O. Vodkin and B. T. Cunningham, *Anal. Chem.*, 2010, **82**, 6854–6861.
- 40 M. G. Moharam and T. K. Gaylord, *J. Opt. Soc. Am.*, 1981, **71**, 811–818.
- 41 P. E. Sheehan, L. J. Whitman, W. P. King and B. A. Nelson, *Appl. Phys. Lett.*, 2004, **85**, 1589–1591.
- 42 J. R. Felts, S. Somnath, R. H. Ewoldt and W. P. King, *Nanotechnology*, 2012, **23**, 215301.
- 43 W. P. King, B. Bhatia, J. R. Felts, H. J. Kim, B. Kwon, B. Lee, S. Somnath and M. Rosenberger, *Annu. Rev. Heat Transfer*, 2013, **16**, 287–326.
- 44 H. Hu, P. K. Mohseni, L. Pan, X. Li, S. Somnath, J. R. Felts, M. A. Shannon and W. P. King, *J. Vac. Sci. Technol., B: Nanotechnol. Microelectron.: Mater., Process., Meas., Phenom.*, 2013, **31**, 06FJ01.
- 45 L. Tian, J. J. Morrissey, R. Kattumenu, N. Gandra, E. D. Kharasch and S. Singamaneni, *Anal. Chem.*, 2012, **84**, 9928–9934.
- 46 L. Tian, E. Chen, N. Gandra, A. Abbas and S. Singamaneni, *Langmuir*, 2012, **28**, 17435–17442.
- 47 I. D. Block, L. L. Chan and B. T. Cunningham, *Sens. Actuators, B*, 2006, **120**, 187–193.
- 48 K. Yu, Y. Tian and T. Tatsuma, *Phys. Chem. Chem. Phys.*, 2006, **8**, 5417–5420.